

Impacts of high-latitude volcanic eruptions on ENSO and AMOC

SI Appendix

Francesco S.R. Pausata^{a,1}, Leon Chafik^{a,b,c}, Rodrigo Caballero^a and David S. Battisti^{d,e}

^a*Department of Meteorology, Stockholm University and Bolin Centre for Climate Research, 10691, Stockholm, Sweden*

^b*NOAA/NESDIS Center for Satellite Application and Research, College Park, MD, 20740*

^c*Cooperative Institute for Climate and Satellites, University of Maryland, College Park, MD, 20740*

^d*Department of Atmospheric Sciences, University of Washington, Seattle, WA, 98195*

^e*UNI Research, 5008 Bergen, Norway*

¹*To whom correspondence should be addressed. Email: francesco.pausata@misu.su.se*

High-latitude eruption simulated by NorESM1-M

The objective of our study is to examine the response of the ocean to a hypothetical large high-latitude volcanic eruption on short- (0-3 years) and long-time scales (up to 60 years from the eruption). We use as a starting point for our study a transient simulation (1850-2005) performed with the Norwegian Earth System Model (NorESM1-M(1, 2)) with online calculation of aerosols and their direct effect and the first and second indirect effects on warm clouds.

The Model

NorESM1-M is an Earth System Model that uses a modified version of the Community Atmospheric Model version 4 (CAM4 (3)), CAM4–Oslo, for the atmospheric part of the model. CAM4–Oslo includes an updated aerosol module that simulates the life cycle of sea salt, mineral dust, particulate sulfate, black and organic carbon (4). CAM4–Oslo has a separate representation of aerosol–radiation and aerosol–cloud interactions. The model uses the finite volume dynamical core for transport calculations, with horizontal resolution 1.9° (latitude) \times 2.5° (longitude) and 26 vertical levels, as in the original CAM4. CAM4–Oslo is coupled with the updated version of the Miami Isopycnic Coordinate Ocean Model – MICOM(5). The sea ice and land models are basically the same as in the Community Climate System Model version 4 – CCSM4 (6).

The model can adequately represent the modern climate variability (2): the northern and southern annular modes, the Madden-Julian Oscillation and the El Niño Southern Oscillation are well-captured in the model. Bellenger et al.²⁸ have shown that NorESM1-M has one of the best simulations of ENSO of all the climate models evaluated in the Coupled Model Intercomparison Project 5 (CMIP5). The metrics used in the evaluation of the model ENSO cycle include the amplitude, spatial structure, frequency spectrum and the seasonality of ENSO, and the strengths of the feedbacks (such as the Bjerknes, heat flux, shortwave feedbacks) responsible for the ENSO

variability. NorESM simulates a vigorous Atlantic Meridional Overturning Circulation (AMOC) compared to other models, being in the upper range of AMOC strengths simulated by CMIP3 models (2, 7). Measured by the maximum in the overturning streamfunction in N. Atlantic, the AMOC in the NorESM is about 30 Sv at 26.5°N, whereas the observed AMOC is about 18-20 Sv (1).

A detailed analysis of NorESM performances is provided in Iversen et al. (2) and for the volcano simulations in Pausata et al. (8).

Experiment design and prescription of forcing

We simulate a hypothetical multi-stage high-latitude volcanic episode by injecting 100 Tg of SO₂ and dust – as an analog for ash – over 8 eruptions, starting on June 1st. Each sub-eruption lasts 4 days, for an overall duration of 4 months (Table S1). The SO₂ injection heights follow the percentage distribution reported in the work of Thordarson and Self (9) for the Laki eruption, the second largest high-latitude volcanic eruption in historical time, occurred in 1783. However, the aim of the paper is not to validate the simulation against the Laki reconstruction, which has been done in Pausata et al. (8), but rather to investigate the short and long term impact of a hypothetical high-latitude eruption.

Table S1: Total amount of SO₂ (Tg) emitted for each of the 4-day long eruption, and its vertical distribution. Maximum emission pressure height $p = 100$ hPa (~15 km).

Eruption date	Jun 1 st	Jun 15 th	Jul 1 st	Jul 15 th	Aug 1 st	Aug 15 th	Sep 1 st	Sep 15 th
Total SO ₂ (Tg)	42	11	11	15	9	5	4	3
100 < p < 150 hPa	5	1	1	2	1	0	0	0
150 < p < 300 hPa	29	8	8	10	6	4	3	2
$p > 300$ hPa	8	2	2	3	2	1	1	1

We have analyzed two sets of ensemble members:

1) ENS_v-A: The volcanic eruption starts from a specific year selected from a transient 156-year climatology (1850-2005). We generate the ensemble members by perturbing the initial condition of that specific year in which the eruption is simulated. Twenty simulations are performed, each for 4 years. Ten of these simulations are extended to 60 years so that we can evaluate the long-term impact of the eruption episode on the AMOC.

2) ENS_{nv}-A: We generate an equivalent cluster of ensemble members with the concentration of volcanic aerosols set to background conditions (historical emissions taken from IPCC AR5 datasets, see Kirkevåg et al. (4)) by perturbing the initial condition used to create the ENS_v. As

in the ENS_v ensemble, 20 4-year simulations are performed, ten of which are extended to 60 years.

The year 1934 of the control simulation was selected as the eruption year for ENS_v : (eruption year: number 01), which is roughly in the middle of the climatology period and features a strong El Niño event, as was the case in 1782/83 before the Laki eruption (10). The only difference between the two clusters is the volcanic forcing. This set-up allows avoiding misinterpretations of ocean heat content changes due to the fact that the model has not reach a full equilibrium (11).

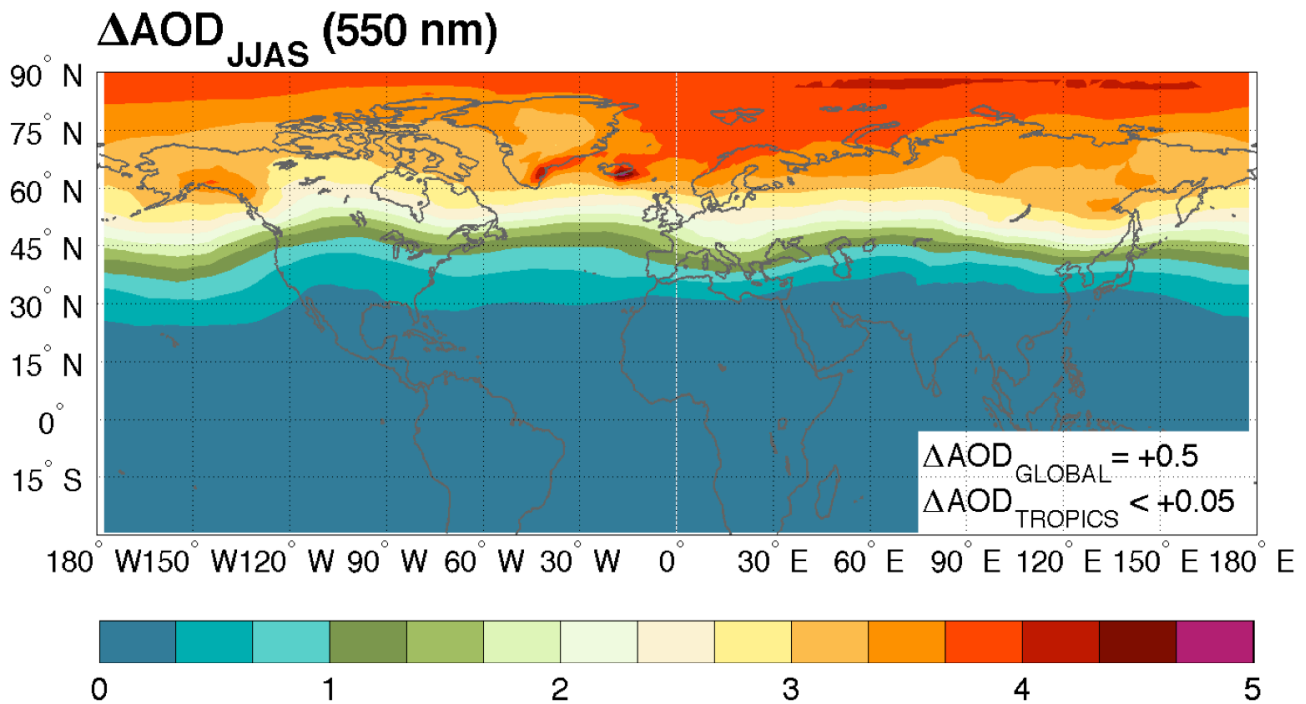


Figure S1: Ensemble average change (ENS_v minus ENS_{nv}) in aerosol optical depth (AOD) at 550 nm calculated for the months of the eruption (June to September). The numbers in the box in the right bottom corner show the global and tropical (between 23°S and 23°N) averaged changes in AOD.

Short-term impacts on ENSO

Our results show that the high-latitude volcanic eruption generates an aerosol plume that is confined to the Northern Hemisphere above $20\text{-}30^\circ\text{N}$ in the months following the eruption, with no direct radiative forcing of the tropical zone (Fig. S1). Nevertheless, a significant strengthening of the El Niño phase takes place, peaking six months after the start of the eruption (i.e. in December), and is followed by a more negative La Niña phase on the second and third year (Fig. 1). The El Niño-like anomaly in the first 9 months from the start of the eruption is caused by the cooling of the Northern Hemisphere, and in particular the cooling of the extra-tropics in the Northern Hemisphere (Fig. S2).

The hemispherically asymmetric cooling leads to a southward shift of the Inter-Tropical Convergence Zone (ITCZ) (Figs. S2 and S3) due to robust and well understood physics (see, e.g.,

(12–14)). The amplitude of the ITCZ shift may be sensitive to the details of the model convection scheme (12), however the response is expected to be qualitatively similar across models.

A southward shift of the zonally averaged ITCZ commences quickly after the start of the eruption (0-3 months) over the Asian continent (where the cooling is strongest and peaks in the summer of the eruption) and the tropical Atlantic, bringing the ITCZ closer to the equator in all three basins by 4-6 months after the start of the eruption (Fig. S3). Since surface easterly winds are weakest under the ITCZ, the equatorward shift over the tropical Pacific implies a weakening of the easterly trade winds along the equator (i.e. a westerly anomaly – Fig. S4). This weakening of the trade winds over the equatorial Pacific leads to a reduction in the east-west temperature contrast across the tropical Pacific and thus begets an El Niño-like anomaly via the Bjerknes feedback (15).

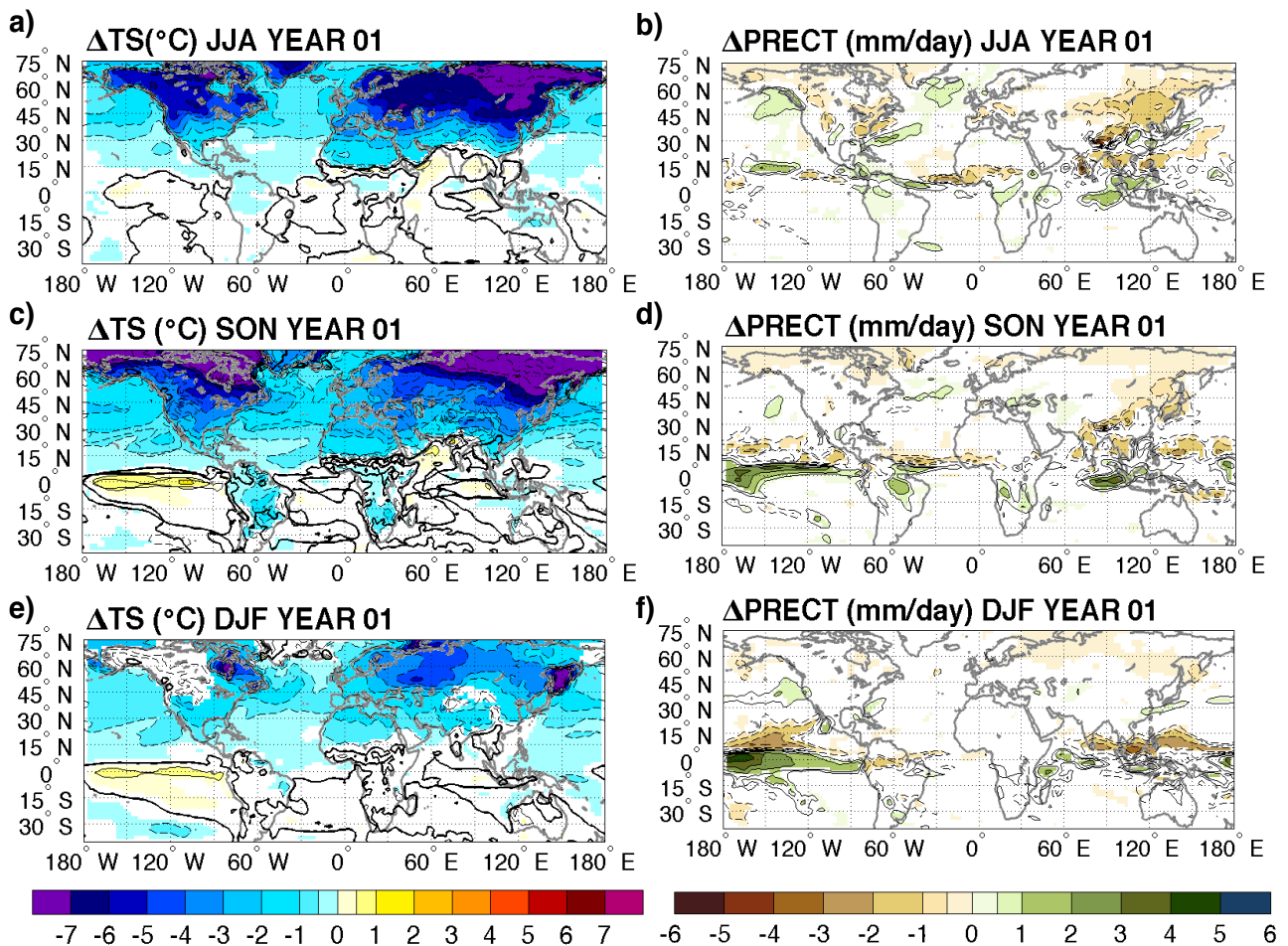


Figure S2: Ensemble average change (ENS_v minus ENS_{nv}) in surface temperature (left) and precipitation (right) caused by the eruption. Changes are calculated for (a-b) 1-3 months (JJA), (c-d) 4-6 months (SON), and (e-f) 7-9 months (DJF) following the start of the eruption. The color shading displays regions where anomalies are significant at the 95% confidence level. The contour intervals (dashed = negative anomalies; solid = positive anomalies) follow the color scale. The bold line in the left panels indicates the 0°C anomaly.

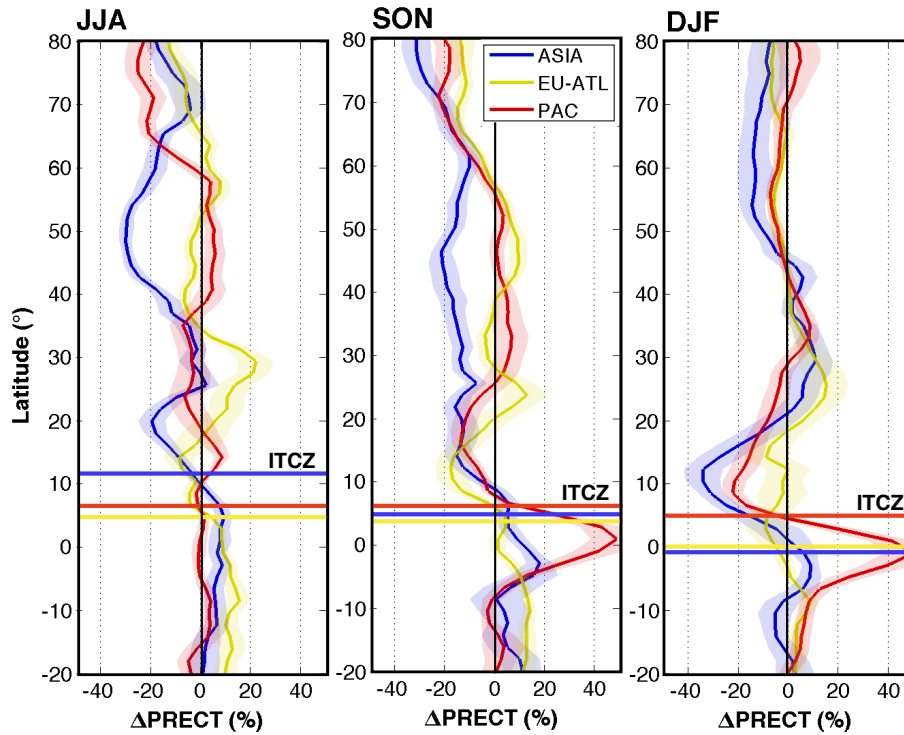


Figure S3: Ensemble average change (ENS_v minus ENS_{nv}) in zonal averaged precipitation (in %) over different geographical regions for 1-3 (a), 4-6 (b) and 7-9 (c) months following the start of the eruption. The regions are: Asia $60^{\circ}E - 150^{\circ}E$; Europe-Atlantic Ocean $90^{\circ}W - 50^{\circ}E$; and the Pacific Ocean $150^{\circ}E - 90^{\circ}W$). The horizontal lines show the average position of the ITCZ in each respective area in the no-volcano ensemble, ENS_{nv} . Shading shows the approximate 95% confidence intervals (twice the standard error of the mean) of the difference between the pairs of experiments that comprise the ensembles.

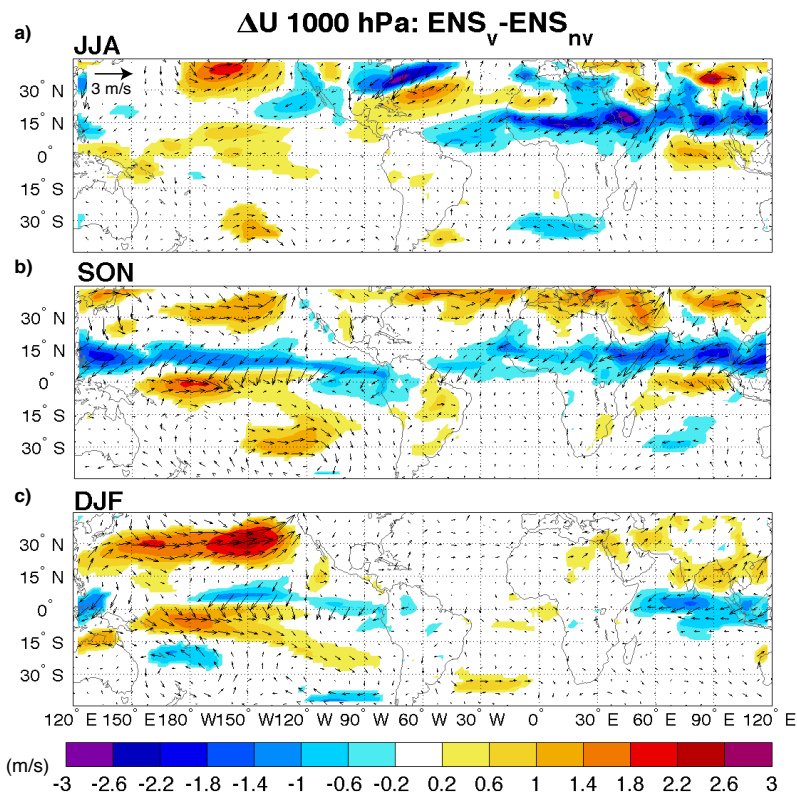


Figure S4: As in Figure S1, but for the change in wind velocity (vectors) and zonal wind speed (shading) at 1000 hPa between ENS_v and ENS_{nv} for (a) 1-3, (b) 4-6, and (c) 7-9 months following the start of the eruption.

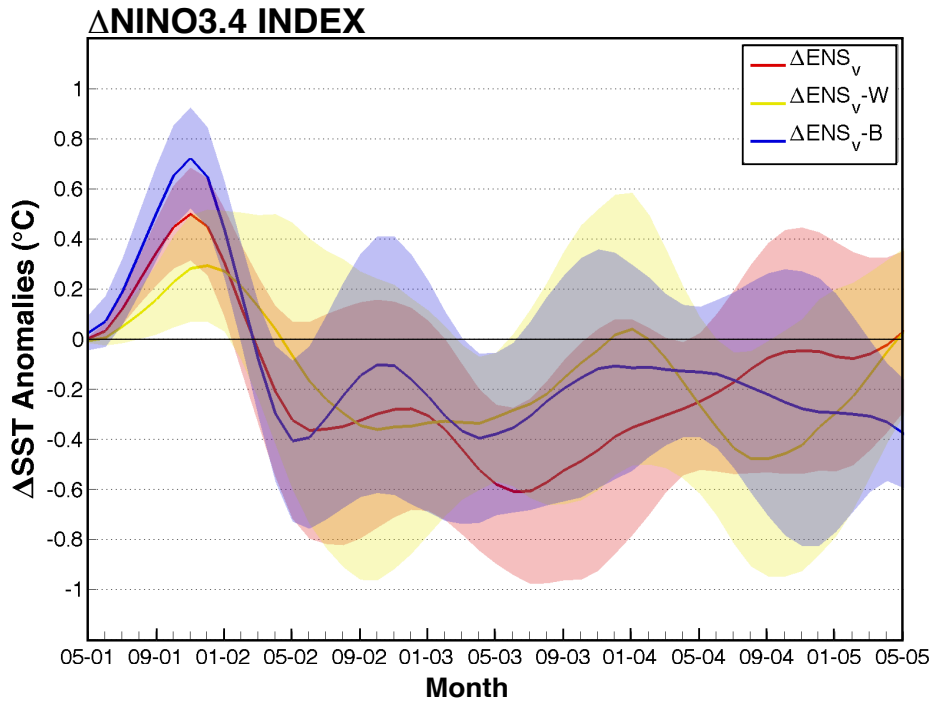


Figure S5: Ensemble average change (ENS_v^* minus ENS_{nv}^*) in the Nino3.4 Index for the strong (100 Tg SO_2 , ENS, red) and weak (33 Tg SO_2 , ENS-W, yellow/brown) eruption with ensemble members starting from a specific year, and for the strong (100 Tg SO_2 , ENS-B, blue) eruption starting in different years. The solid line indicates the ensemble average response and the shading denotes the approximate 95% confidence intervals (twice the standard error of the mean) of the difference between the pairs of experiments that comprise the ensembles.

To investigate whether the El Niño-like response depends on the pre-existing ocean state, we performed an additional experiment, in which each pair of experiments (volcano and no-volcano) start from identical initial conditions in the ocean and atmosphere, but the initial conditions for each pair of experiments are taken five years apart from a control (no volcano simulation) experiment (e.g., 1860, 1865, ..., 1960). Hence, each pair of experiments starts from a unique phase of ENSO. Each experiment is integrated for four years. The difference between each pair of experiments thus illuminates the impact of the volcano that erupted during a unique phase of ENSO. The difference between the ensemble average of the volcano experiments (ENS_v-B) and the corresponding ensemble average of the no-volcano experiments ($ENS_{nv}-B$) measures the average impact of the volcano starting from different ENSO states. An El Niño-like anomaly develops in response to this eruption in a very similar fashion as the El Niño-like anomaly that was generated in response to the eruption that started during an El Niño event – i.e., in the ENS_v (Fig. S5). However, the magnitude of the anomaly is larger in the ENS-B than in the ensemble of experiments, all starting from El Niño conditions (ENS). A detailed examination of the ENS-B members reveals that the El Niño-like response to the eruption seems to be stronger starting from La Niña and neutral conditions (12 cases in ENS-B) compared to starting from El Niño years (8 cases in ENS-B). This explains why the response in the ENS-B is larger compared to ENS. However, the number of El Niño/La Niña

events is small to be conclusive and further investigation is required to confirm these results. We also performed an ensemble (n members=10) of integrations in which the strength of the imposed multi-event eruption was reduced by 1/3 to about 33 Tg of SO₂, (ENS_{v-W}), which results in a weaker cooling over the Northern Hemisphere. The El Niño-like anomaly in response to the eruption is weaker than the anomaly generated by the larger eruption (because the cooling of the NH is reduced), but it is still significant and clearly visible (Fig. S5). Therefore, the El Niño-like anomaly in the first months following the start of the eruption strongly depends on the amplitude of the eruption (Fig. S5).

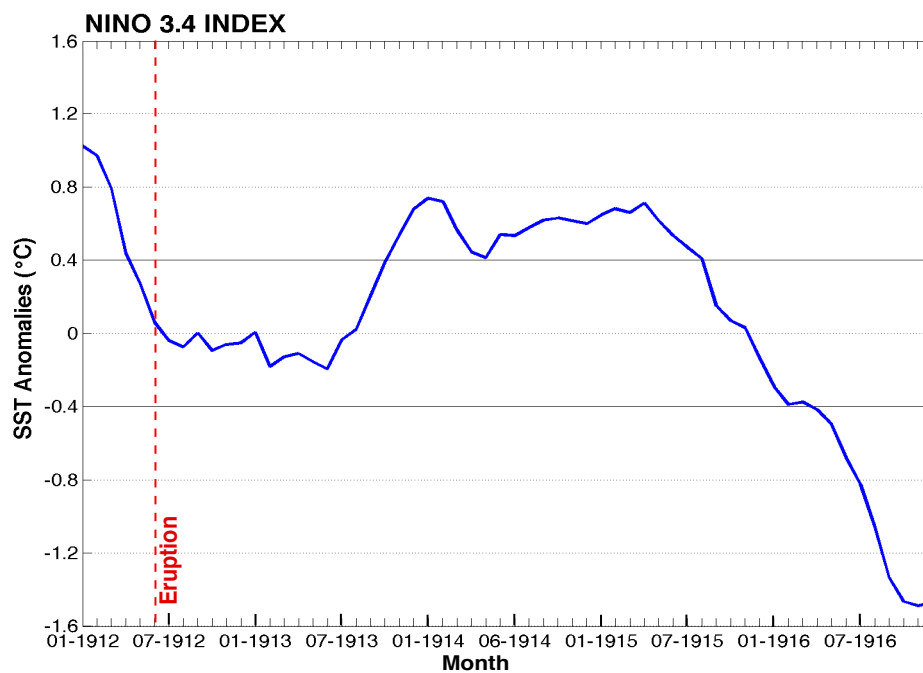


Figure S6: Nino3.4 Index for the period Jan 1912 – Dec 1916, calculated using SST anomalies (°C) normalized to 1971–2000 from Hadley Centre SST data set (HadISST1). A 5-month running mean has been applied to remove uncoupled intraseasonal variations in SST.

Our model results are difficult to compare to past strong high-latitude eruptions given their scarce number during the last hundred and fifty years when reanalysis of the sea surface temperature (SST) are available. Furthermore, it is difficult to verify whether a given eruption has or not triggered an El Niño response since it is not possible to know how the climate system would have behaved without such eruption. Nevertheless, when analyzing the Nino3.4 index behavior in the months preceding and following the largest high-latitude eruption of the 20th century (Katmai in 1912), it is intriguing that El Niño event that peaked in January of 1912, six months prior to the Katmai eruption was immediately followed by near normal conditions in the tropical Pacific (Fig. S6) rather than the La Niña conditions that normally occur after El Niño events. The near normal conditions were then followed by an El Niño event starting a year after the eruption. Therefore, the ENSO behavior following the Katmai eruption is consistent with our findings. Furthermore, the El Niño

conditions preceding the Laki eruption were further strengthened in the winter of 1783-84 (6 to 9 months after the beginning of the eruption) as shown by tree-ring data (10, 16) in agreement with our findings.

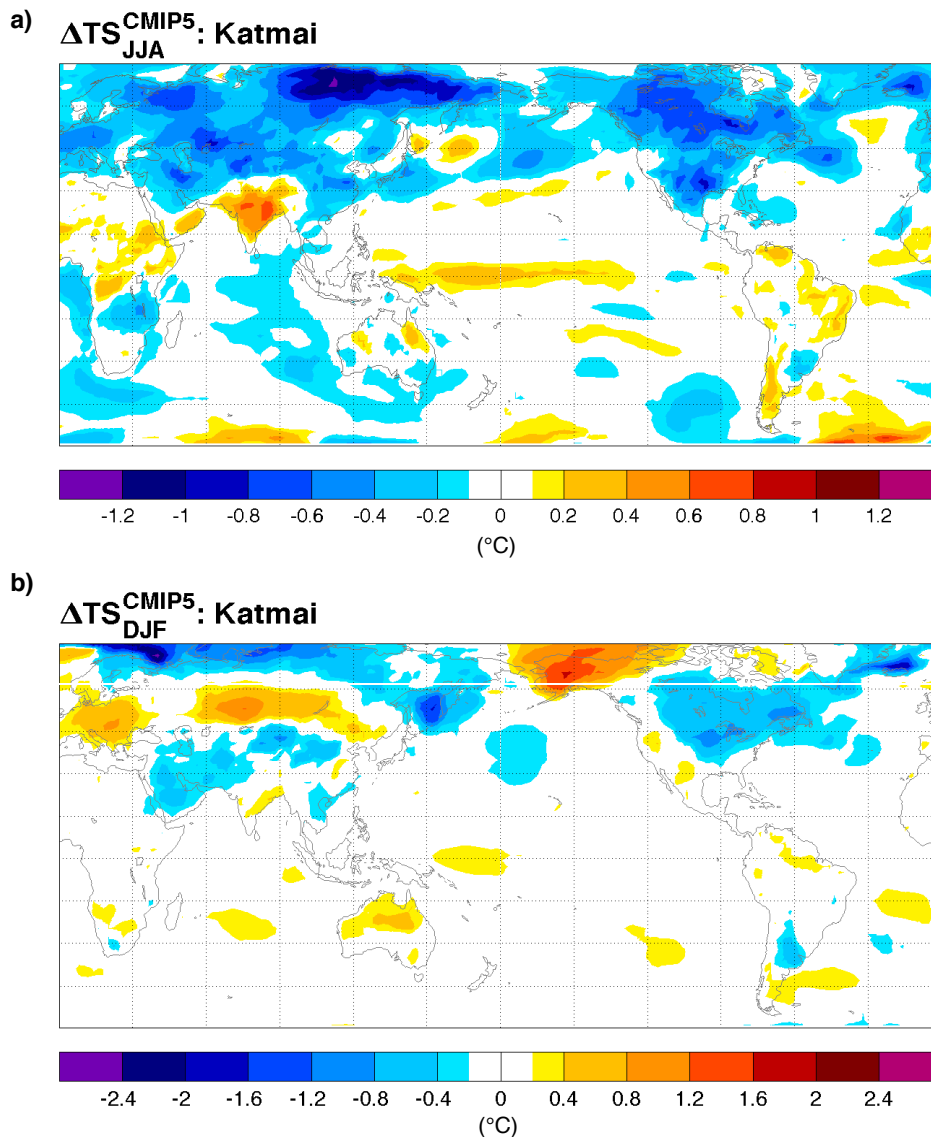


Figure S7: Surface temperature anomalies for the summer (JJA) and the winter (DJF) following the Katmai eruption (June 1912) in 15 CMIP5 models.

Finally, we performed a multimodel composite response to Katmai in the historical (20th Century) simulations in the CMIP5 archive. In forming our composite, we included results from all the CMIP5 models that feature realistic ENSOs in their control simulations: specifically, we used the 15 models that best simulate ENSO with spatial and temporal characteristics consistent with observational constraints according to the criteria used in Bellenger et al. (17). We find that the multimodel-mean Northern Hemisphere cooling for the seasons following the eruption is much smaller than in the simulated Laki-type eruption presented in this study, though similar in spatial structure (cf. Fig. S7 and S2). Hence, one would expect an El Niño-like anomaly 4-9 months after

the eruption, though weaker than in our study. The surface temperature composites over the historical CMIP5 simulations show that for the seasons immediately following the Katmai eruption, significant warm anomalies are in fact present in the equatorial Pacific in the Nino4 and partially Nino3.4 regions (Fig. S7).

We must note, however, that the CMIP5 historical simulations are not ideal for investigating the impact of large high-latitude volcanic eruptions. To unambiguously assess the impact of the volcanic eruption on ENSO two types of simulations are necessary: a control experiment without the eruption and an experiment with an eruption imposed — both starting from the same initial conditions at the onset of the eruption. The latter experiments are included in the historical simulations using the CMIP5 models, but unfortunately the accompanying control experiments were not performed as part of CMIP5. Furthermore, the CMIP5 historical simulations only include one large high-latitude volcanic eruption (Katmai); with such a small sample it is difficult to isolate the volcanic impact without the complementary control (no volcano) experiments, even using alternative statistical approaches (e.g., (18)).

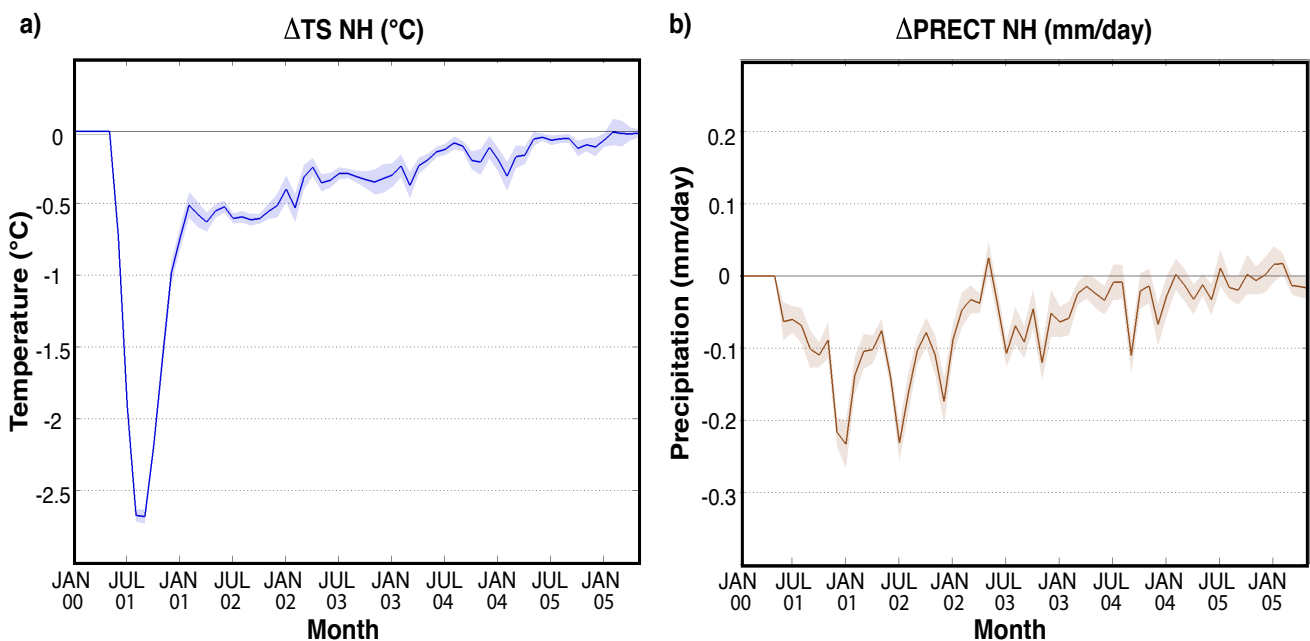


Figure S8: Ensemble average change (ENS_v minus ENS_{nv}) in NH averaged surface air temperature (a) and precipitation (b), between ENS_v and ENS_{nv} . Shading shows the confidence intervals (twice the standard error of the mean) of the change seen in all twenty pairs of experiments

Long-term impacts on ocean circulation and ENSO

AMOC response

The Atlantic Meridional Overturning Circulation (AMOC) index is the maximum in the zonally averaged overturning stream function in the North Atlantic between 30°N and 60°N and between 500 and 2000 m depth.

The Atlantic Meridional Overturning Circulation (AMOC) shows a brief (less than 6 months) weakening after the volcanic eruption, followed by a progressive AMOC strengthening that takes place and peaks between 5 and 10 years after the eruption (Fig. 3a). The maximum AMOC anomaly is about 1.5 Sverdrup (Sv; $1 \text{ Sv} = 10^6 \text{ m}^3/\text{s}$). Thereafter, the AMOC starts to slow down and reaches a minimum anomaly of a $\sim -1 \text{ Sv}$ about 35-40 years after the eruption. The AMOC remains significantly weaker than the control ENS_{nv} from 25 years after the eruption until the end of the analyzed period, with a slow recovery over the last decade of the simulations. The negative radiative forcing from volcanic aerosols results in a cold surface temperature anomaly that develops during the first ~ 3 years (Fig. S5). These cold SST anomalies are gradually transferred into the deep ocean by mixing and convection (Fig. 3b). The general cooling on the NH is accompanied by reduced precipitation (Figs. S3 and S8b) and consequently reduced river runoff at high latitudes of the Northern Hemisphere. Therefore, more saline and hence denser upper ocean conditions develop at higher latitudes of the Northern Hemisphere (Fig. S9). In the Atlantic, both colder ocean temperatures and enhanced salinity destabilize the water column, leading to enhanced oceanic convection (Fig. S10), and a spin-up of the AMOC. The strengthening of the AMOC is followed by a progressive weakening of the AMOC, which reaches a minimum about 35-40 years after the eruption after which it stays below normal until the end of the analyzed period (60 years).

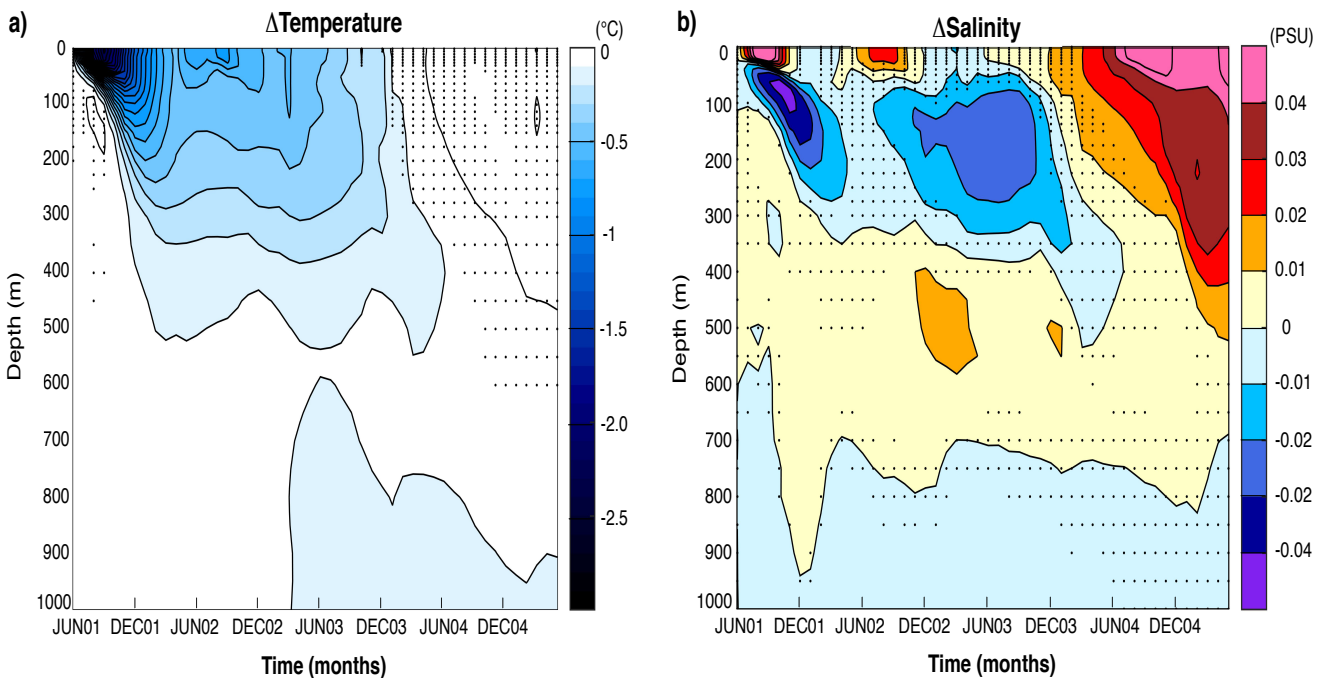


Figure S9: Ensemble average change (ENS_{v} minus ENS_{nv}) in temperature (a) and salinity (b) as a function of time in the North Atlantic (averaged over 25° to 57° W, and 42° to 57° N). The stippled areas denoted grid-boxes in which the difference is not significant at 95% confidence level using a t test.

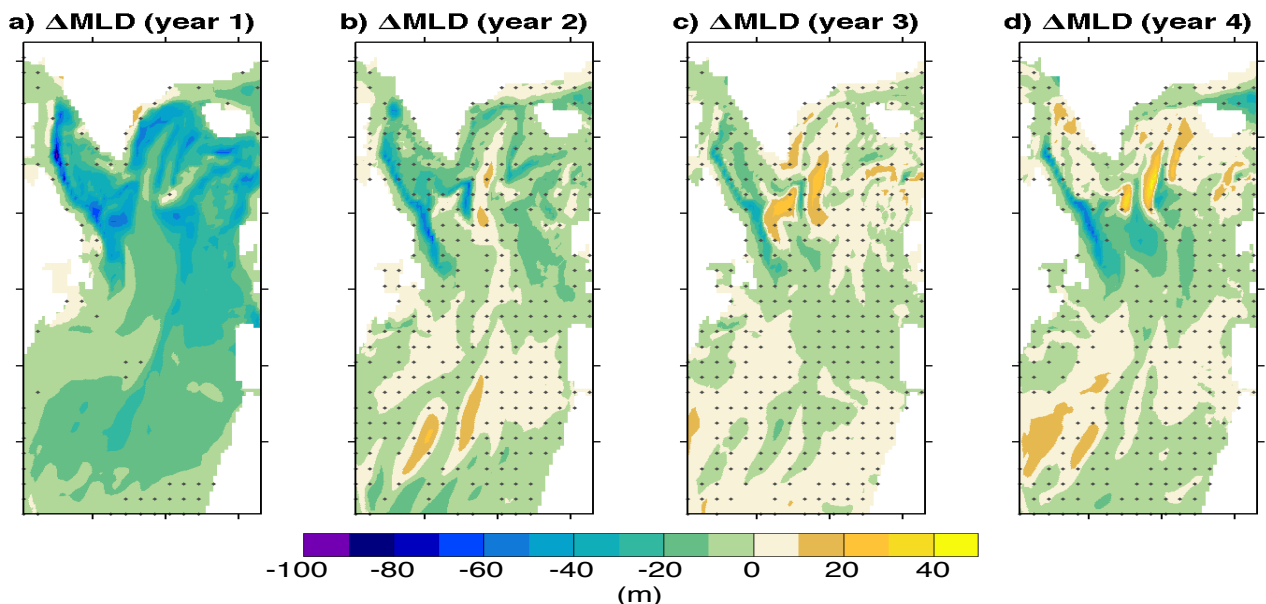


Figure S10: Ensemble average change (ENS_v minus ENS_{nv}) in mix layer depth over the North Atlantic for the first 4 years following the eruption. Negative numbers indicate a deeper mixed layer. Changes in mixed-layer depth are good proxy for convection strength over the North Atlantic. The stippled areas denoted grid-boxes in which the difference is not significant at 95% confidence level using a t test.

ENSO response

The ENSO variance is affected by changes in the strength of the AMOC: during years 5-25 after the volcanic eruption when the AMOC is increased in amplitude, the ENSO variance is increased (by $\sim 7\%$) relative to that in the no-volcano ensemble (Table S2); during years 26-45 when the AMOC is weaker than normal, the variance in ENSO is reduced by $\sim 16\%$.

To investigate whether the ENSO frequency is also influenced by AMOC variability, we adopt two different approaches to determine the length of the ENSO cycle in NorESM: the characteristic ENSO period and the average El Niño return time.

To estimate the characteristic ENSO period, we first concatenated the Nino3.4 index from all 10 experiments for each time period (210, 200 and 150 years) in each ensemble ensuring continuity in the Nino3.4 anomalies. Using these time series, we estimate a characteristic period by doubling the time lag for which the autocorrelation of the Nino3.4 index is at the extreme negative value. The minimum in the autocorrelation for the Nino3.4 index represents the lag time between El Niño and the following La Niña state (or vice versa) and hence, represents half ENSO cycle. Therefore, to determine the ENSO cycle we double the minimum lag time in the autocorrelation.

To estimate the average El Niño return time we first find the start date of all the El Niño events that happen in each epoch (1-25 years, 26-60 years) and in each simulation in the ensemble; an El Niño event is deemed to occur when the Nino3.4 anomalies exceed $+0.4$ °C for at least 6 consecutive months. For each epoch, we then calculate the return time between all El Niño events in each of the 10 simulations that comprise the ensemble, and average these return times. The

AMOC is stronger (weaker) in the volcano simulations than in the no-volcano simulations in the first 25 years (years 25-60) after the volcanic eruption.

To assess the significance of the difference in characteristic ENSO period and the average El Niño return time between the volcano and no-volcano ensemble we use the bootstrap technique in which we randomly subsample 100 periods of 25 uninterrupted years for both ensembles. To verify whether the changes in the mean characteristic ENSO period and the average El Niño return time are statistically significant at 95% confidence level we apply the t test to the subsample generated through the bootstrap technique.

For years 5-25 after the eruption, the autocorrelation analysis indicates there is a slight increase in the ENSO period due to the volcanic impact on the AMOC (Table S3), whereas a six-month decrease in the ENSO period is found 26-45 years after the eruption associated with the volcano-induced reduction in AMOC.

Table S2: Standard deviation ($^{\circ}\text{C}$) of the Nino3.4 index for the volcano (ENS_v) and no-volcano (ENS_{nv}) ensemble members for different time periods after the eruption (year 1). ENS_v standard deviations greater (less) than ENS_{nv} are shown in red (blue) and in bold when significant at 95% confidence level using the F test.

PERIOD	NINO3.4 index	
	STANDARD DEVIATION ($^{\circ}\text{C}$)	
	ENS_{nv}	ENS_v
5 to 60 years	0.85	0.82
5 to 25 years	0.81	0.87
26 to 45 years	0.89	0.75
46 to 60 years	0.85	0.82

Table S3: Characteristic ENSO period and return time for El Niño events found in the volcano and no-volcano ensemble.

PERIOD	NINO3.4 FREQUENCY			
	Autocorrelation		Average return time	
	ENS_{nv}	ENS_v	ENS_{nv}	ENS_v
1 to 25 years	3 yrs 2 mnts	3 yrs 4 mnts	3 yrs 9 mnts	3 yrs 9 mnts
26 to 60 years	3 yrs 6 mnts	3 yrs 0 mnts	3 yrs 8 mnts	3 yrs 7 mnts
1 to 60 years	3 yrs 4 mnts	3 yrs 2 mnts	3 yrs 9 mnts	3 yrs 8 mnts

Although the ensemble average return time does not change significantly due to the volcanic eruption (Table S3), an examination of the distribution of return times for each epoch and each ensemble reveals an 11% decrease in the short-cycle (<25th percentile) and 5% decrease in the long-cycle periods (>75th percentile – Table S4) in the first 25 years after the eruption. The last 35 years

of the simulation (years 26-60) suggest instead more frequent (14%) very short or very long cycles (12% – Table S4) owing to the volcanic eruption.

Table S4: Percentiles of Nino3.4 event average return time calculated for the concatenated Nino3.4 time series for the ENS_{nv} and its changes (%) for each epoch in the ENS_v .

PERIOD		NINO 3.4 FREQUENCY					
		Percentiles					
		25 th		50 th		75 th	
		yrs	mnts	yrs	mnts	yrs	mnts
1 to 25 yrs	ENS_{nv}	2	4	3	6	5	3
	ENS_v	+11%		–		-5%	
26 to 60 yrs	ENS_{nv}	2	5	3	1	4	3
	ENS_v	-14%		–		+12%	
1 to 60 yrs	ENS_{nv}	2	5	3	4	4	11
	ENS_v	-7%		-5%		-2%	

Relation between AMOC strength and ENSO variability

Several studies have highlighted the influence of the AMOC on ENSO variability owing to both atmospheric teleconnections (19–24) and oceanic waves that transmit thermocline signals from the North Atlantic to the tropical Pacific (25–27). However, the time scales associated with these teleconnections are very different: the atmospheric influence can be transmitted from the tropical Atlantic into the tropical Pacific in few weeks, whereas the oceanic teleconnections have a time scale of a few decades (23–25).

In order to test whether the simulated changes in the amplitude and frequency of ENSO are indeed related to the strength of the AMOC in our model, we isolate epochs in the no-volcano ensemble in which the AMOC index is unusually strong and unusually weak, as defined when the AMOC index is above the 85th and below the 15th percentile, respectively, for at least 48 consecutive months. We have chosen the 85th and 15th percentiles in order to get a mean AMOC change that is comparable to the change between the stronger (5 to 25 years) and weaker (26 to 45 years) AMOC periods associated with the volcanic eruption (see Fig. 3a): The mean difference between the strong and the weak AMOC in the no-volcano ensemble is ~ 2.55 Sv, whereas the changes in the AMOC difference between the volcano and no-volcano ensemble in the two periods is ~ 2.45 Sv.

First, we calculate the change in the standard deviation of the tropical Pacific SST anomalies for the strong and the weak AMOC epochs in the no-volcano ensemble and between years 5 to 25 years and years 26 to 45 due to the volcanic eruption. Strong AMOC phases are clearly associated

with increased variability in the Tropical Pacific (Fig. S11a). The shape and the magnitude of the changes are remarkably similar to those induced by the volcanic eruption (Fig. S11b).

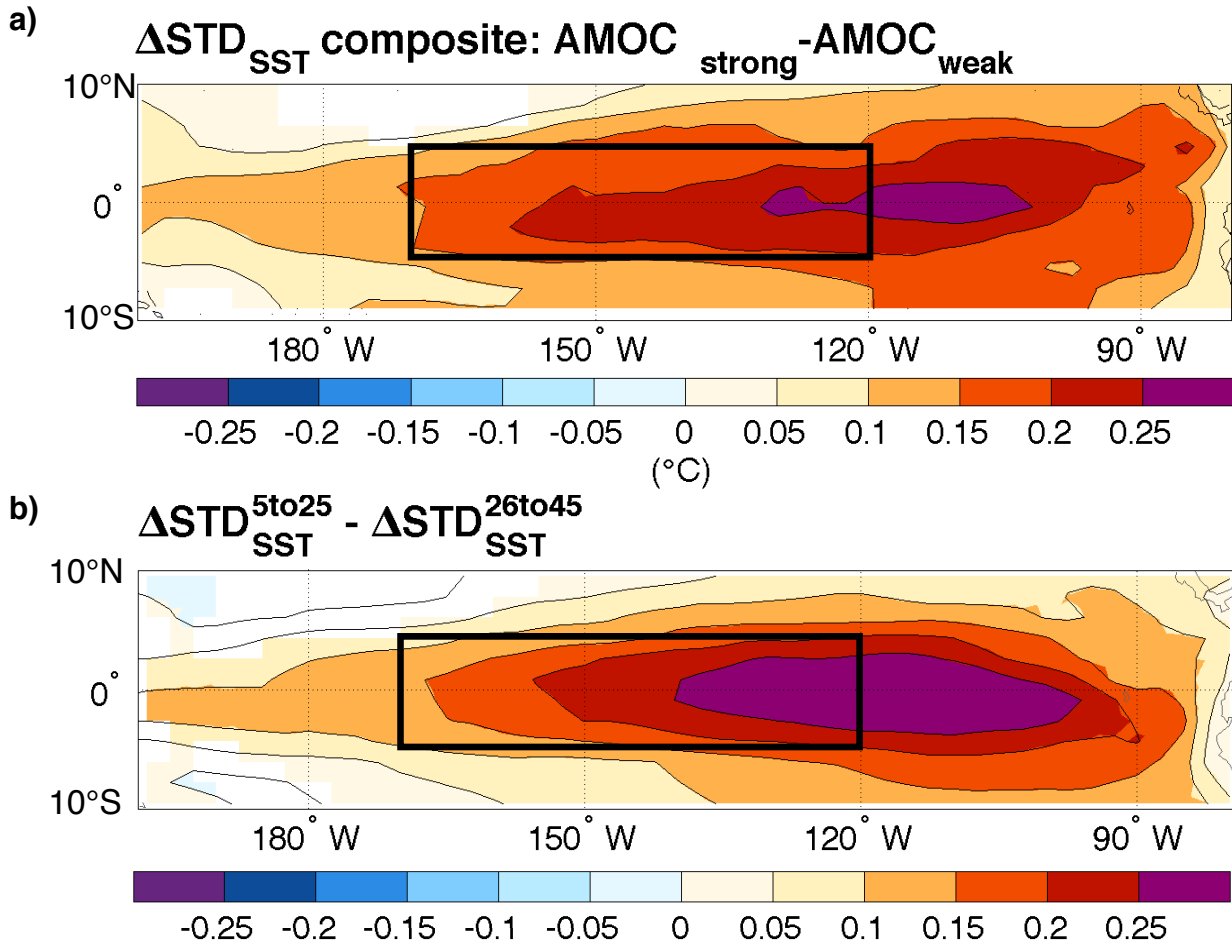


Figure S11: a) Composite of the SSTD standard deviation changes (in °C) between strong and weak AMOC periods in the ENS_{nv} simulations. The strong and weak AMOC periods are defined as periods in which the AMOC maximum anomalies are outside the 15th-85th percentiles for at least 48 consecutive months. b) Difference in SSTD standard deviation changes between the period 5-25 years and 26-45 years after the eruption (i.e. the difference between panel a (strong AMOC anomalies) and b (weak AMOC anomalies) in Figure 3). The color shading displays changes that are significant at the 95% confidence level using the F test. The contour interval is 0.05°C (dashed = negative anomalies; solid = positive anomalies; the zero line is omitted). The box delimitates the Niño3.4 area.

To investigate whether the mechanisms affecting the ENSO variance between the years 5-25 and between years 26-45 after the eruption are similar to those associated with the unforced multidecadal AMOC variability, we analyze the climatological mean state changes in the tropical Pacific in the two set-ups (Fig. S12). The changes in the climatological SSTD associated with the change from low to high AMOC in the unforced simulation are similar to those associated with the changes in AMOC due to the volcano; in particular, the cooling over the maritime continent and the warming south of the equator in the central/southeast Pacific, thereby decreasing slightly the east-

west temperature gradient over the tropical Pacific (Fig. S12 cf. panels a and b). Periods of stronger AMOC also show a southward displacement of the ITCZ in the Pacific and a decrease in rainfall in the western tropical Pacific; elsewhere, changes in the tropical Atlantic associated with high and low AMOC periods are qualitatively different in the unforced experiment compared to the volcanically forced changes. The surface wind changes show a strengthening of the westerlies in Northern Hemisphere high-latitudes, a weakening in the Southern Hemisphere high-latitudes and a strengthening over the Equatorial Pacific in both set-ups.

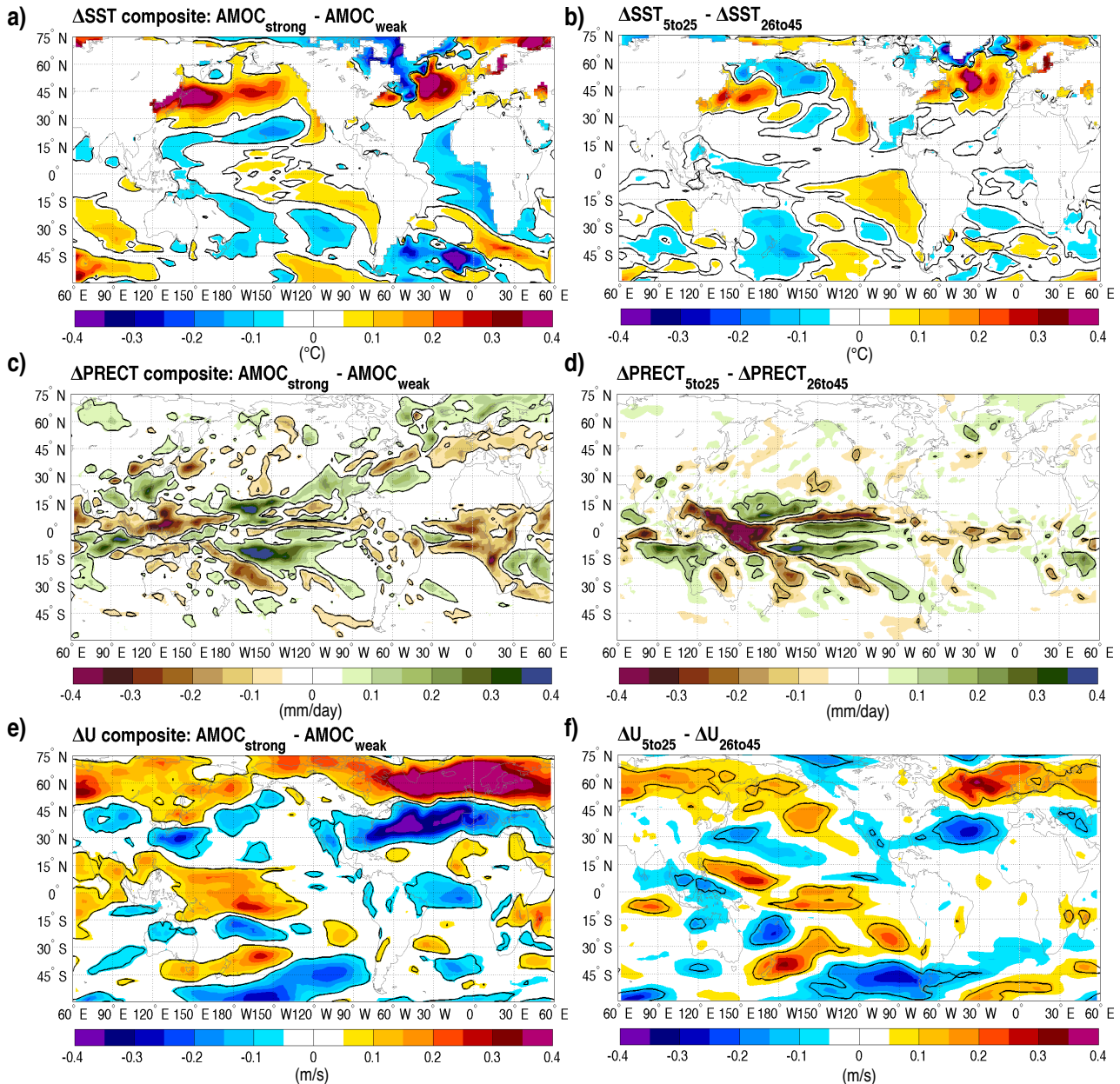


Figure S12: Composite of the change in climatological SST (a), precipitation (c) and 1000 hPa zonal wind (e) between strong and weak AMOC periods in the ENS_{nv} simulations. The strong and weak AMOC periods are defined as periods in which the AMOC maximum anomalies are outside the 85th-15th percentiles for at least 48 consecutive months. Panels (b), (d) and (f) are as in panels (a), (c) and (e), respectively, only for the climatological change between years 5 to 25 and years 26 to 45 after the eruption. The contours show the areas significant at 95% confidence level using the t test.

We note that a back-of-the-envelope calculation shows that the asymmetry in the hemispheric average temperature is sufficiently small that the physics outlined in Kang et al. (12) is unlikely to be apropos to the multidecadal changes in the tropical Pacific atmosphere and ocean that are associated with the changes in AMOC strength, forced or unforced. Strong AMOC periods increase the asymmetry in the hemisphere-averaged temperature in the Northern Hemisphere compared to the Southern Hemisphere by only $\sim 0.06^\circ\text{C}$. Using a typical regression value that relates a change in surface temperature to a change in surface heat flux ($\sim 15 \text{ W/m}^2/^\circ\text{C}$), this implies a change in the cross equatorial ocean heat flux of about 0.015PW . Assuming this heat flux is balanced by an equal but opposite a cross equatorial atmosphere, the results of Donohoe et al. (28) imply the AMOC would cause a latitudinal change in the zonal average ITCZ of barely 5km .

Stronger AMOC phases in both the unforced simulations and during years 5-25 of the volcanic simulations feature – albeit with a different pattern – a more stratified thermocline than in the weak AMOC phases of the unforced and forced simulations (Fig. S13) and a more responsive zonal wind (Fig. S14). Stronger AMOC results in a shoaling and a stratification of the Pacific thermocline (Fig. S13). As shown by Russell and Gnanadesikan (29), a stronger ocean stratification in the tropical Pacific and more responsive zonal winds are coupled with enhanced ENSO variability.

The increase in ENSO variance when the AMOC strengthens may then be attributable to a stronger Bjerknes feedback that results from changes in the structure of the climatological thermocline in the Pacific. The latter could be accomplished by either the adjustment of global scale oceanic waves or by changes in the climatological wind stress curl over the Pacific that stem from the large-scale atmospheric adjustment to AMOC induced changes in the tropical Atlantic. Our results indeed show increased ocean stratification in the equatorial Pacific and a stronger Bjerknes feedback (Fig. S14) associated with stronger AMOC (Fig. S13). The changes in the zonal mean thermocline depth over the equatorial Pacific (Fig. S13) are comparable in magnitude to previous modeling estimates. For example, in Timmermann et al. (25) the thermocline depth in the Pacific undergoes variations of about 4 meters ($\sim 4 \text{ m}$) associated to AMOC changes of $\sim 15 \text{ Sv}$. Dong and Sutton (17) show a change of the thermocline depth in the equatorial Pacific of up to 10 m and temperature anomaly at 150 m depth of up to $0.75\text{-}1^\circ\text{C}$ following a AMOC weakening of 20 Sv .

To conclude, overall these results indicate that volcanically induced changes in the AMOC can give rise to multidecadal variations in ENSO activity. Further studies are necessary to investigate in detail the interplay among the changes in the Pacific mean state presented here and how they can lead to the simulated changes in ENSO variability.

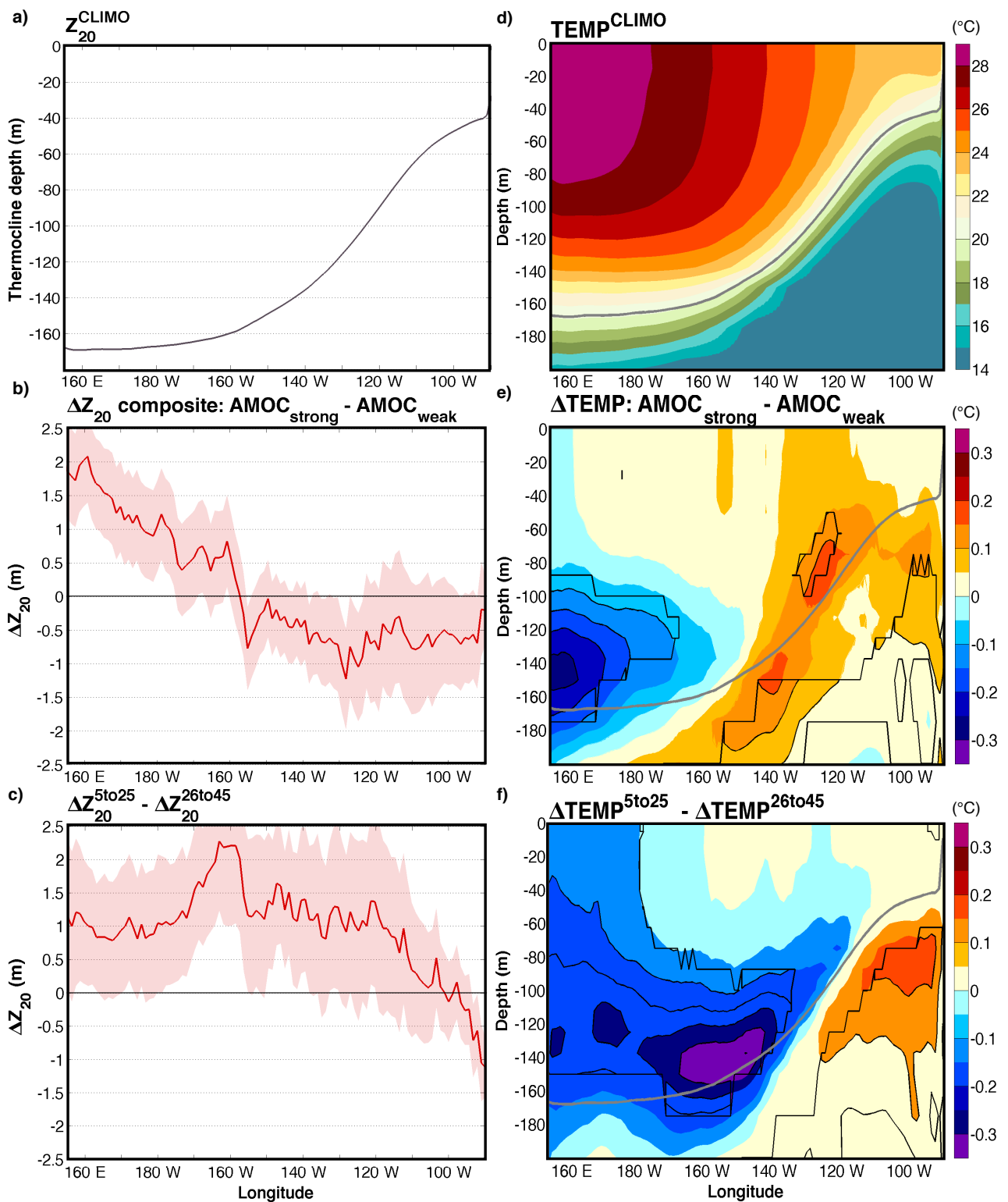


Figure S13: a) Climatological thermocline depth (as defined using the 20°C isotherm Z_{20}), b) the anomalies between stronger and weaker AMOC periods and c) between the changes in the 5 to 25 year and 26 to 45 year periods, averaged over the tropical Pacific (3°S – 3°N). Positive values means shoaling and negative values a deepening of the thermocline. Shading shows the confidence intervals (twice the standard error of the mean). d) Climatological annual mean temperature (°C), the anomalies e) between stronger and weaker AMOC periods and f) between the changes in the 5 to 25 year and 26 to 45 year periods, averaged over the tropical Pacific (3°S – 3°N). The contours in panels e) and f) show significant difference at 95% confidence level using a *t* test.

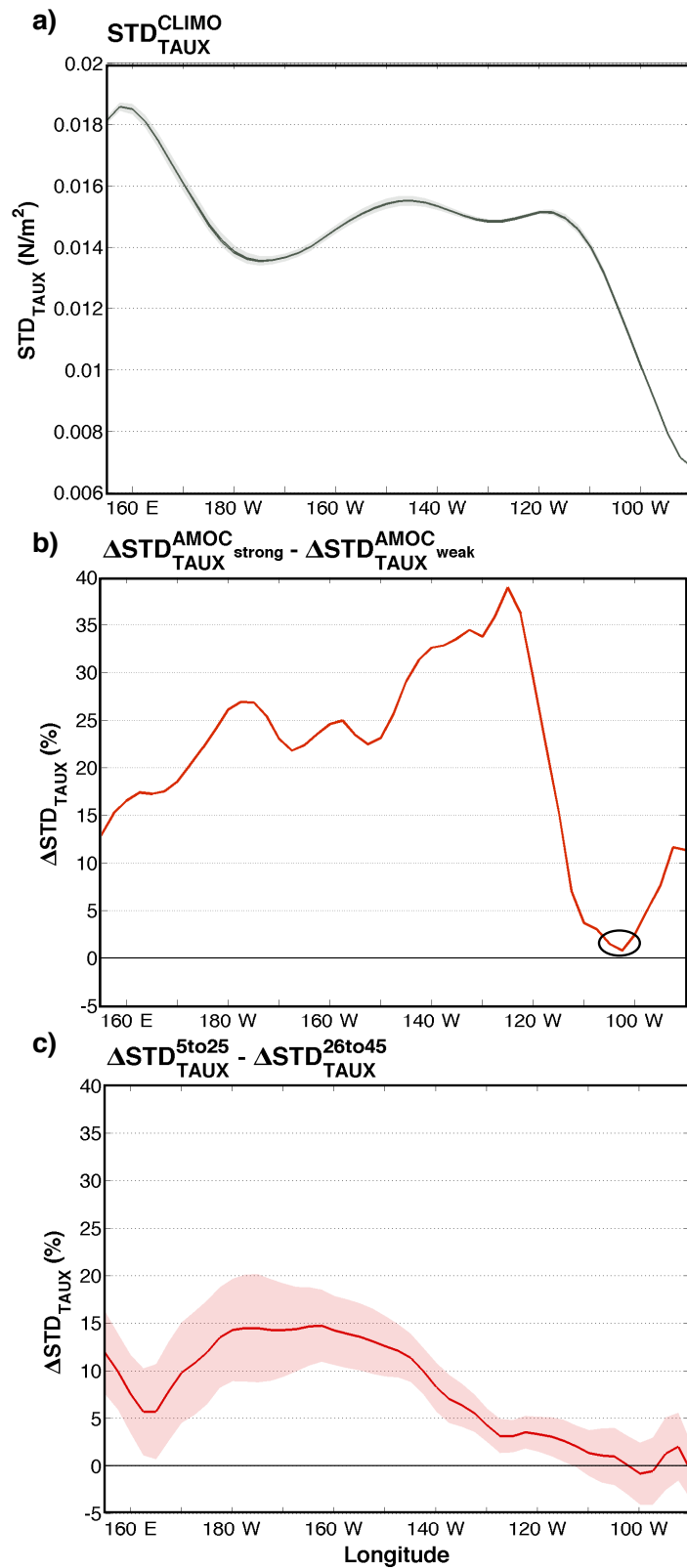


Figure S14: a) Climatological standard deviation of the zonal wind stress (TAUX), averaged over the tropical Pacific (3°S – 3°N). b) Change in the standard deviation of zonal wind stress associated with strong vs. weak periods of AMOC in the unforced (no-volcano) simulation. c) Change in the standard deviation of zonal wind stress during the period 5 to 25 years after the eruption (with anomalously strong AMOC) minus the change in the period 26 to 45 year periods after the eruption (with anomalously weak AMOC). In panels a) and c) the shading shows the approximate 95% confidence intervals (twice the standard error of the mean). In panel b) the anomalies are significant in the entire domain at 95% confidence level using the F test, except in the region encircled.

References

1. Bentsen M, et al. (2013) The Norwegian Earth System Model, NorESM1-M – Part 1: Description and basic evaluation of the physical climate. *Geosci Model Dev* 6(3):687–720.
2. Iversen T, et al. (2013) The Norwegian Earth System Model, NorESM1-M – Part 2: Climate response and scenario projections. *Geosci Model Dev* 6(2):389–415.
3. Neale RB, et al. (2013) The Mean Climate of the Community Atmosphere Model (CAM4) in Forced SST and Fully Coupled Experiments. *J Clim* 26(14):5150–5168.
4. Kirkevåg A, et al. (2013) Aerosol-climate interactions in the Norwegian Earth System Model - NorESM1-M. *Geosci Model Dev* 6:207–244.
5. Assmann KM, Bentsen M, Segsneider J, Heinze C (2010) Model Development An isopycnic ocean carbon cycle model. *Geosci Model Dev* 3:143–167.
6. Gent PR, et al. (2011) The Community Climate System Model Version 4. *J Clim* 24(19):4973–4991.
7. Medhaug I, Furevik T (2011) North Atlantic 20th century multidecadal variability in coupled climate models: sea surface temperature and ocean overturning circulation. *Ocean Sci* 7(3):389–404.
8. Pausata FSR, Grini A, Caballero R, Hannachi A, Seland Ø (2015) High-latitude volcanic eruptions in the Norwegian Earth System Model: the effect of different initial conditions and of the ensemble size. *Tellus B* 67(26728).
9. Thordarson T, Self S (2003) Atmospheric and environmental effects of the 1783–1784 Laki eruption: A review and reassessment. *J Geophys Res* 108(D1):4011.
10. Cook E, Krusic P (2004) North American Drought Atlas, NOAA Paleoclimatol., Boulder, Colo. Available at: <http://iridl.ldeo.columbia.edu/SOURCES/.LDEO/.TR.L/.NADA2004/.pdsi-atlas.html>
11. Gregory JM (2010) Long-term effect of volcanic forcing on ocean heat content. *Geophys Res Lett* 37(22):L22701.
12. Kang SM, Held IM, Frierson DMW, Zhao M (2008) The Response of the ITCZ to Extratropical Thermal Forcing: Idealized Slab-Ocean Experiments with a GCM. *J Clim* 21(14):3521–3532.
13. Schneider T, Bischoff T, Haug GH (2014) Migrations and dynamics of the intertropical convergence zone. *Nature* 513(7516):45–53.
14. Chiang JCH, Friedman AR (2012) Extratropical Cooling, Interhemispheric Thermal Gradients, and Tropical Climate Change. *Annu Rev Earth Planet Sci* 40(1):383–412.
15. Bjerknes J (1969) Atmospheric teleconnections from the equatorial Pacific. *Mon Weather Rev* 97(3):163–172.
16. D’Arrigo R, Seager R, Smerdon JE, LeGrande AN, Cook ER (2011) The anomalous winter of 1783–1784: Was the Laki eruption or an analog of the 2009–2010 winter to blame? *Geophys Res Lett* 38(5):L05706.
17. Bellenger H, Guilyardi E, Leloup J, Lengaigne M, Vialard J (2014) ENSO representation in climate models: from CMIP3 to CMIP5. *Clim Dyn* 42(7–8):1999–2018.
18. Maher N, McGregor S, England MH, Sen Gupta A (2015) Effects of volcanism on tropical variability. *Geophys Res Lett* 42(14):6024–6033.
19. Dong B, Sutton RT (2007) Enhancement of ENSO Variability by a Weakened Atlantic Thermohaline Circulation in a Coupled GCM. *J Clim* 20(19):4920–4939.
20. Dong B, Sutton RT, Scaife AA (2006) Multidecadal modulation of El Niño–Southern Oscillation (ENSO) variance by Atlantic Ocean sea surface temperatures. *Geophys Res Lett* 33(8):L08705.
21. Dong B-W, Sutton RT (2002) Adjustment of the coupled ocean-atmosphere system to a sudden change in the Thermohaline Circulation. *Geophys Res Lett* 29(15):18–1–18–4.
22. Zhang R, Delworth TL (2005) Simulated Tropical Response to a Substantial Weakening of the Atlantic Thermohaline Circulation. *J Clim* 18(12):1853–1860.
23. Atwood AR (2015) Mechanisms of tropical Pacific climate change during the Holocene. PhD dissertation (University of Washington).
24. Timmermann A, et al. (2007) The Influence of a Weakening of the Atlantic Meridional Overturning Circulation on ENSO. *J Clim* 20(19):4899–4919.
25. Goodman PJ (2001) Thermohaline Adjustment and Advection in an OGCM*. *J Phys Oceanogr* 31(6):1477–1497.
26. Cessi P (2004) Global seiching of thermocline waters between the Atlantic and the Indian-Pacific Ocean Basins. *Geophys Res Lett* 31(4):L04302.
27. Timmermann A, An S-I, Krebs U, Goosse H (2005) ENSO Suppression due to Weakening of the North Atlantic Thermohaline Circulation. *J Clim* 18(16):3122–3139.
28. Donohoe A, Marshall J, Ferreira D, Mcgee D (2013) The Relationship between ITCZ Location and Cross-Equatorial Atmospheric Heat Transport: From the Seasonal Cycle to the Last Glacial Maximum. *J Clim* 26(11):3597–3618.
29. Russell AM, Gnanadesikan A (2014) Understanding Multidecadal Variability in ENSO Amplitude. *J Clim* 27(11):4037–4051.